Water Resources Research

RESEARCH ARTICLE
10.1029/2024WR037425

Special Collection:
Hydrogeodesy: Understanding changes in water resources using space geodetic observations

Key Points:

- Geodetic observations reveal widespread and remarkable subsidence, with rate up to ∼120 mm/yr in North China Plain during 2015–2019
- A comprehensive evaluation of aquifer properties and groundwater storage changes in the North China Plain is conducted using geodetic and hydrological data
- Trend of subsidence in parts of North China Plain has slowed due to implementation of South-to-North Water Diversion Project

Supporting Information:

Supporting Information may be found in the online version of this article.

Correspondence to:

J. Sun,
sunjianbao@ies.ac.cn

Citation:

Li, M., Sun, J., Xue, L., Shen, Z.-K., Li, Y., Zhao, B., & Hu, L. (2025). Characterizing aquifer properties and groundwater storage at North China Plain using geodetic and hydrological measurements. *Water Resources Research*, *61*, e2024WR037425. https://doi.org/10.1029/2024WR037425

Received 29 FEB 2024
Accepted 2 FEB 2025

Author Contributions:

Conceptualization: Jianbao Sun, Lian Xue, Zheng-Kang Shen
Data curation: Mingjia Li, Bin Zhao, Leyin Hu
Formal analysis: Mingjia Li, Jianbao Sun
Funding acquisition: Jianbao Sun

Characterizing Aquifer Properties and Groundwater Storage at North China Plain Using Geodetic and Hydrological Measurements

Mingjia Li[1,2,3], Jianbao Sun[1], Lian Xue[2,4], Zheng-Kang Shen[2,5], Yuexin Li[6], Bin Zhao[7], and Leyin Hu[8]

[1]State Key Laboratory of Earthquake Dynamics and Forecasting, Institute of Geology, China Earthquake Administration, Beijing, China, [2]School of Earth and Space Science, Peking University, Beijing, China, [3]Department of Earth and Space Sciences, Southern University of Science and Technology, Shenzhen, China, [4]Hongshan Geophysical National Observation and Research Station, Peking University, Beijing, China, [5]Department of Earth, Planetary, and Space Sciences, University of California, Los Angeles, Los Angeles, CA, USA, [6]Division of Geological and Planetary Sciences, California Institute of Technology, Pasadena, CA, USA, [7]Key Laboratory of Earthquake Geodesy, Institute of Seismology, China Earthquake Administration, Wuhan, China, [8]Beijing Earthquake Agency, Beijing, China

Abstract Climatic and anthropogenic changes are reshaping global water resources, with the North China Plain (NCP) experiencing significant surface subsidence due to severe groundwater overexploitation over the past half-century. In this study, we integrate data from Interferometric Synthetic Aperture Radar, Global Navigation Satellite System, and hydraulic head measurements observed in 2015–2019 to investigate aquifers' physical properties and corresponding changes in groundwater storage in NCP. Geodetic measurements indicate seasonal and long-term deformation patterns. The amplitude of seasonal variation of deformation is up to 25 mm with phase lag behind the seasonal variation of water head. The integration of geodetic and hydrological data indicates that local aquifer storativity and clay lens thickness are $0.67 \times 10^{-3} - 14.38 \times 10^{-3}$ and $0.15 - 1.98$ m, respectively. The average long-term subsidence due to sustained water storage loss is about 29 mm/yr, with a peak rate of ∼120 mm/yr. Even though all regions show a long-term ongoing subsidence, the subsidence trend has slowed in about half of the NCP, which can be attributed to the impact of the South-to-North Water Diversion (SNWD) Project, especially in areas near the SNWD aqueducts. Moreover, we find a disparity in subsidence rates between Hebei and Shandong Provinces, reflecting the impact of different groundwater exploitation management in mitigating the subsidence. This research underscores the effectiveness of combining geodetic and hydrological data for assessing groundwater circulation and optimizing groundwater management.

Plain Language Summary Groundwater overexploitation and the resulting surface subsidence have become growing concerns in the developing world, especially in the North China Plain, where cities have seen increases in population and water use over the last half-century. To address this challenge, the South-to-North Water Diversion Project was launched, with water diversion starting in 2014. However, questions remain about the groundwater storage capacity of the plain and the project's effectiveness in alleviating the groundwater depletion. Answers to these questions are pivotal for the understanding of the groundwater system, enabling efficient groundwater management, and mitigation of related hazards. Here, we combine geodetic and hydrological data to deduce the aquifer's physical properties and groundwater storage change patterns. Our results highlight the unique characteristics of groundwater sub-regions and establish connections to the sub-regions with their hydro-sedimentation history by discerning deformation patterns attributed to various hydrogeological processes. Furthermore, we provide convincing evidence of the mitigation in groundwater storage depletion attributable to the South-to-North Water Diversion Project and quantify the results. Overall, our results confirm that, although subsidence continues across the North China Plain, the trend has slowed in specific areas, notably in major cities along the routes of the diversion project.

1. Introduction

Groundwater is a critical source of fresh water worldwide, yet it is becoming rapidly depleted in some regions due to the demands of agricultural irrigation and economic development (Aeschbach-Hertig & Gleeson, 2012). Regions such as the Central Valley in California (Faunt et al., 2016), the Indo-Gangetic Plain in India (Watto &

Investigation: Mingjia Li, Jianbao Sun, Lian Xue, Zheng-Kang Shen
Methodology: Mingjia Li, Jianbao Sun, Lian Xue, Yuexin Li
Project administration: Jianbao Sun
Resources: Jianbao Sun
Software: Mingjia Li, Jianbao Sun
Supervision: Jianbao Sun, Zheng-Kang Shen
Validation: Mingjia Li
Visualization: Mingjia Li
Writing – original draft: Mingjia Li
Writing – review & editing: Jianbao Sun, Lian Xue, Zheng-Kang Shen, Yuexin Li

Mugera, 2016), and the North China Plain (NCP) (Zhang, Fei, et al., 2009) are experiencing severe challenges with groundwater storage (GWS) depletion. The GWS depletion and the subsequent irreversible decline in GWS capacity can threaten ecosystems and economies, including reduction of agricultural products, damage to buildings from land subsidence (Ohenhen et al., 2024; Shirzaei et al., 2021), and destruction of ecosystems due to saltwater intrusion and increase of flood susceptibility (Herrera-García et al., 2021; Jain et al., 2021). Therefore it is essential to monitor GWS variations, and assess the effectiveness of groundwater management policies in groundwater management (Jasechko et al., 2024). Additionally, investigating aquifer properties, such as storativity and clay lens thickness, are also important for constructing numerical models of hydraulic flows to quantitatively assess groundwater resources (Sharma et al., 2017; Yao et al., 2019). These steps are fundamental in ensuring sustainable groundwater use.

GWS change can be estimated from the change of groundwater level and aquifer characteristics traditionally. These data are typically measured from field observations of piezometers or wells and laboratory experiments on core samples from aquifers (Kruseman et al., 1970). Inadequate spatial and temporal coverage of monitoring networks restricts the estimation. Large scale monitoring of GWS can use surveillance observations from the Gravity Recovery and Climate Experiment (GRACE) satellite, which monitors changes of the Earth's gravity field (e.g., Feng et al., 2013; Rodell & Reager, 2023). However, the method's coarse spatial resolution (~300 km) restricts its use primarily to large-scale studies (Feng et al., 2018). The GWS change can cause surface uplift or subsidence (Poland & Ireland, 1988), which can be well captured using geodetic methods with high spatial resolution (e.g., 100 m), such as the Interferometric Synthetic Aperture Radar (InSAR) and Global Navigation Satellite System (GNSS). Integration of hydraulic head and geodetic measurements can improve the spatial resolution and accuracy of GWS at a regional scale (Hung et al., 2012; Motagh et al., 2017). This method also facilitates the measurement of aquifer properties, such as storativity and clay lens thickness, with efficient data acquisition across large regions. Measuring aquifer properties using surface deformation aligns very well with those from traditional methods, which typically require pumping/injection tests. For example, Jiang et al. (2018) combined InSAR and hydraulic head measurements to reveal a spatially heterogeneous storativity pattern in central Cangzhou, consistent with findings from pumping tests. Previous studies have also successfully applied this method to examine land subsidence and hydrological properties in rapidly developing regions, such as California (Chaussard et al., 2014; Schmidt & Bürgmann, 2003), Colorado (Chen et al., 2016), and Utah (Hu & Bürgmann, 2020; Hu et al., 2018) in the United States.

The NCP, located in the northern part of central-east China, has experienced critical reduction of GWS and extensive subsidence over last decades (Cai, 2008; Gong et al., 2018; Liu & Xia, 2004). Detection of large-scale land subsidence of NCP caused by groundwater over-use serves as a compelling example for the effectiveness of application of space geodetic technology. Recent space geodetic data have revealed severe subsidence due to groundwater withdrawal around urban centers in NCP, such as Beijing (Gao et al., 2015; Li et al., 2022), Tianjin (Liu et al., 2016), and Cangzhou (Jiang et al., 2018) over the past decade. However, the spatiotemporal characteristics of the surface subsidence in the NCP have not been fully studied. Obtaining reliable InSAR deformation time-series results across such large regions with intensive agricultural activities remains challenging, leaving gaps in our comprehension of NCP's hydrological-induced deformation pattern, aquifer properties and GWS variation. Moreover, there is still a lack of comprehensive assessment using InSAR time series data for the effect of the South-to-North Water Diversion (SNWD) Project, which is a renowned project to mitigate GWS depletion in China. Furthermore, the integration of geodetic and hydrological measurements in the NCP has not been extensively researched, resulting in a limited understanding of hydraulic processes in this region.

In this study, we construct a time series of InSAR observations of the NCP from 2015 to 2019 using Persistent Scatterer Interferometry (PSI) method, further constrained by GNSS data. We extract seasonal and long-term patterns from the deformation data, and estimate the aquifer storativity and clay lens thickness combining with hydraulic head measurements. In addition, we estimate the high spatial resolution GWS changes, and quantitatively assess the fulfillment of the SNWD Project. Our study demonstrates how human activities have impacted, in both positive and negative ways, on the GWS across various geographical and hydrological units in China. The results of this study will provide a more accurate reference for monitoring GWS changes and managing the SNWD Project to achieve groundwater sustainability in NCP. The methods and findings should also be applicable to similar highly stressed aquifers worldwide.

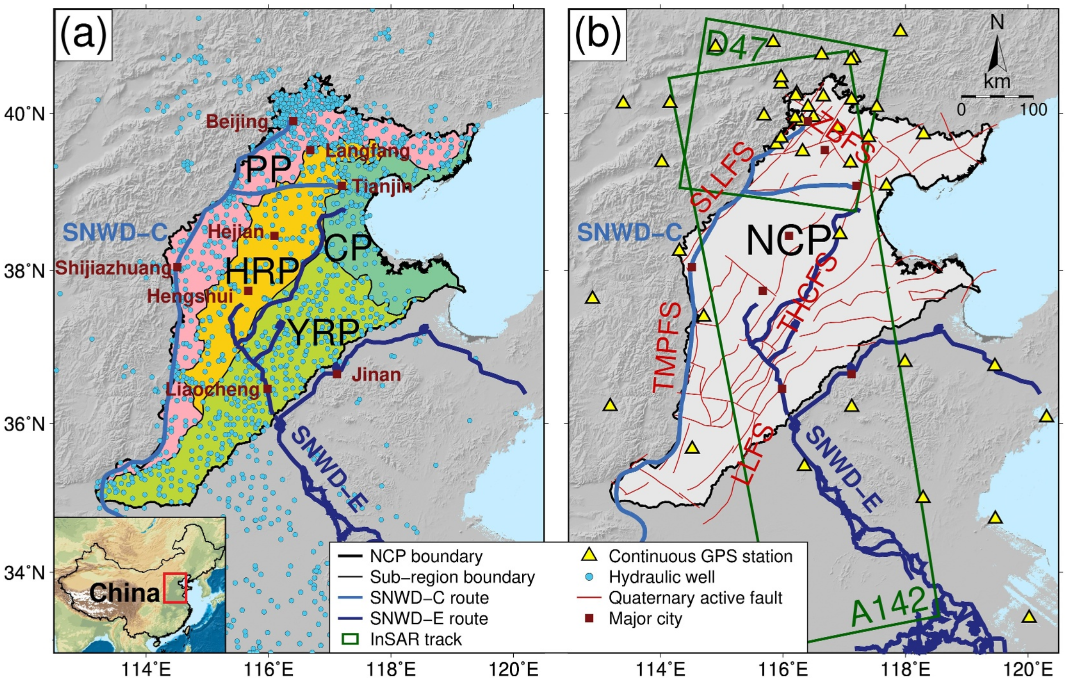

Figure 1. (a) Hydrological setting of NCP. The hydraulic wells are marked as cyan dots, and the groundwater sub-regions are named as the piedmont plain (PP), Hai River plain (HRP), ancient Yellow River plain (YRP), and coastal plain (CP), respectively (Meng et al., 2011; Zhang, Luo, et al., 2009). The East and Central Routes of SNWD Project are traced in dark and light blue, respectively, while major cities are marked with dark red squares. (b) Tectonic setting of NCP and geodetic data coverage. Yellow triangles denote continuous GPS (CGPS) stations providing reference for InSAR data. Green boxes show the spatial footprints of ascending and descending InSAR tracks. Red lines indicate quaternary active faults extracted from Deng (2003), including the Zhangjiakou-Bohai (ZBFS), Liaocheng-Lankao (LLFS), Tangshan-Hejian-Cixian (THCFS), Sanhe-Laishui-Lingshou (SLLFS), and Taihang Mountain Piedmont (TMPFS) fault systems.

2. Hydrological Settings

The NCP is a part of the Bohaiwan Basin region located in the northern part of central-east China (Xu & Ji, 2015), where groundwater constitutes the main water supply and meets 69.4% of the total water consumption (Zhang, Fei, et al., 2009). The groundwater system of NCP spans the entire plain, and can be divided into four sub-regions according to river drainage and sedimentary condition (Figure 1a) (Zhang, Luo, et al., 2009). The piedmont plain (PP) area contains coarse-grained sand and gravel aquifers, while the Hai River plain (HRP) area is dominated by the Hai River and its upstream tributaries. The water conductivity of the HRP area is notably lower than that of the PP area. Aquifer of the ancient Yellow River plain (YRP) is similar to that of the HRP, but has a denser clay layer due to the historically flooding and sediment-rich past of the Yellow River. Besides, the coastal plain (CP) area, which is shaped by seawater intrusion, has the clay-rich aquifer, restricting infiltration from rain and surface water (Meng et al., 2011).

The NCP is renowned for its extensive corn, wheat, and cotton cultivation (Xu & Ji, 2015; Y. Zhang et al., 2020), resulting in a large agricultural water demand that accounts for over 70% of the total water consumption. Alarmingly, groundwater meets more than 75% of this demand, resulting in its severe over-exploitation (Zhang et al., 2018). Recognizing this groundwater crisis, in 2002, the South-to-North Water Diversion (SNWD) Project was initiated to channel water from water-rich southern China to the water-starved northern China (Liu & Zheng, 2002). Since 2014, the SNWD Project's East Route (Figure 1b) has been channeling water from the Yangtze River to over 20 southeastern NCP cities. Meanwhile, the SNWD Project's Central Route (Figure 1b) has been transporting water at a rate of ~9.5 $\mathrm{km}^3/\mathrm{yr}$, from the Danjiangkou Reservoir of the Hanjiang River to northern municipalities such as Beijing and Tianjin since 2014 (http://nsbd.mwr.gov.cn/). Due to the effect of SNWD Project, the deep groundwater level in certain urban areas has shown significant recovery after 2014, with an increase of about 1~2 m/yr (Yang et al., 2021). Specifically, the diverted water to Beijing increased the mean groundwater depth by 3 m there during 2014–2019 (Long et al., 2020).

3. Geodetic and Hydrological Data

3.1. InSAR Data

We analyze data from two Synthetic Aperture Radar tracks obtained from the Sentinel-1A/1B satellites of European Space Agency. This data set covers the period from June 2015 to June 2019 and comprises 92 ascending images from track 142 and 96 descending images from track 47. We use the GAMMA software (Werner et al., 2000) to generate single-look interferograms, all of which are formed with respect to a single reference image for each track. To achieve optimal spatio-temporal coherence, we choose the reference images at the date of 10 December 2017 for track 142 and 27 November 2017 for track 47, ensuring the perpendicular baselines no more than 150 m (Figure S1 in Supporting Information S1). Then we use 30-m Shuttle Radar Topography Mission digital elevation model to remove the topographic phase (Farr et al., 2007).

3.2. GNSS Data

We acquire our GNSS (GPS) data set from two separate sources: the Crustal Movement Observation Network of China (CMONOC) project and the Beijing Continuously Operating Reference Station (BJCORS) network. Specifically, we collect both CGPS and campaign GPS data from the CMONOC, as well as CGPS data from the BJCORS networks measured in and around NCP. The CMONOC data set comprises measurements from 35 CGPS stations monitored 1999–2017, while the BJCORS data set includes measurements from 14 CGPS stations observed 2015–2019. Among these CGPS stations, 30 stations are situated in our study area (Figure 1b). Moreover, subsets of data from 432 CMONOC campaign GPS sites measured each year from 1998 to 2018 in NCP are collected and processed.

GPS data are processed using the GAMIT/GLOBK software (Herring et al., 2010). Subsequently, we anchor the horizontal GPS velocity to the Eurasia reference frame, based on the plate relative motion rotation pole parameters (Wang et al., 2022; Zhao et al., 2017). The same transformation is applied to the CGPS time series data. Lastly, we obtain a continuum horizontal velocity field by interpolating the horizontal velocities of the continuous and campaign GPS stations using the Velocity Interpolation to Strain Rates method (Shen et al., 2015), with outliers removed.

3.3. Hydraulic Head Data

The hydraulic head observations are from multiple sources. The data set includes daily measurements from 105 confined wells collected during 2015–2019 by the China Earthquake Network Center. It also includes monthly measurements from an additional 559 confined wells taken during 2005–2018 by the National Earth System Science Data Center, National Science & Technology Infrastructure of China (http://www.geodata.cn). Furthermore, the data set has measurements from 581 confined wells and 811 unconfined wells collected during 2018–2019 by the National Groundwater Monitoring Center of China, with the sampling rate of 5 days. Additionally, monthly measurements from 70 confined wells and 48 unconfined wells taken during 2005–2016 are adopted from *the China Groundwater Level Yearbook for Geo-environmental Monitoring*. It is worth noting that majority of the wells in the NCP water level observation networks uses digital pressure sensors with observation errors no greater than 10 mm, as reported by Liu et al. (2018).

Given the diversity of the well water level data originating from various sources, we consolidate the data from wells within 100 m of each other into single site observations. After filtering out outliers with significant noise, 472 observation sites are identified within the InSAR data coverage area (Figure 1b). Among these sites, 300 have only confined aquifer wells, 126 have only unconfined aquifer wells, and only 46 feature both confined and unconfined aquifer wells. The spatial distribution of these sites and their hydraulic head time series are provided in Supporting Information S1 (Figures S2 and S3).

4. Methods

4.1. InSAR Time Series Processing and Vertical Deformation Inversion

To analyze the InSAR data, we utilize the PSI method (Ferretti et al., 2000, 2001; Hooper et al., 2004) to overcome decorrelation problem, a particular challenge in the vegetation-rich NCP. This method identifies Persistent Scatterer (PS) pixels whose echo is dominated by a single scatterer in a series of interferograms, effectively mitigating decorrelation and resulting in a dense PS pixels distribution across the study area. Compared to the small baseline InSAR method, PSI can reduce phase unwrapping errors by using a single reference image and avoid spatial filtering that could introduce noise from non-dominant scatterers (Hooper et al., 2012), and ensure spatial-temporal coherence in vegetation-rich regions. To generate the time series, we use the StaMPS software (Hooper et al., 2012), which can effectively identify PS targets in crop-dense terrains without man-made structures, excelling in its 3-D phase unwrapping strategy. To efficiently derive the full-resolution distributions of PS pixels across NCP for the first time, we apply a parallel processing strategy to reduce computation time. This approach involves dividing the study area into overlapping patches (958 patches for track 47 and 420 patches for track 142) and using a multi-node computing framework to process the data. Choosing the amplitude dispersion threshold value of 0.4, we identify approximately 36 million and 13 million PS pixels for ascending and descending tracks, respectively. To enhance reliability during the unwrapping process, we then downsample the spatial distribution of PS pixels to ∼200 m.

Another main challenge in acquiring the accurate deformation time series in NCP is estimating and reducing the atmospheric phase screen (APS). Here we use a two-tier correction method: the first-order APS is estimated using the ERA5 global atmosphere model (Hersbach et al., 2020), representing the climatic regional-scale and stablely temporal varying parts of the APS, while the residual APS is estimated using the Common Scene Stacking (CSS) method (Tymofyeyeva & Fialko, 2015), including small-scale and high-frequency components of the APS. Specifically, we use the TRAIN Matlab software package (Bekaert et al., 2015) to estimate the first-order APS based on ERA5 model, and the MCANDIS Matlab software package (Wang & Fialko, 2018) to estimate the residual APS and suppress stochastic noise based on the CSS method. To improve the accuracy, we exclude the first and last three image from the InSAR time series due to their limited observation epochs used for data stacking. Figures S4 and S5 in Supporting Information S1 show the unwrapped phase time series with and without atmospheric corrections. Our two-tier correction method effectively removes 74.3% and 53.9% APS for two tracks relative to the GNSS displacement time series, particularly during the rainy summer season.

We use CGPS data as reference to correct for errors related to orbital or other long-wavelength effects in the InSAR data (Shen & Liu, 2020; Zhao et al., 2017). We estimate the 2-D linear trend correction for each InSAR interferogram using least-squares regression at multiple CGPS sites. During this process, we calibrate the InSAR time series using the CGPS time series and remove the long-wavelength errors. Using the sites within the InSAR coverage area or within 20 km of the boundary, we utilize 20 chosen CGPS sites for ascending track 142, and 18 sites for descending track 47 (Figure S6 in Supporting Information S1). Comparing InSAR and CGPS time series (Figure S7 in Supporting Information S1) and assessing root mean square error (RMSE), the mean RMSE for ascending track 142 decreases from 9.77 to 5.12 mm, representing a 47.6% noise reduction (Table S1 in Supporting Information S1). For descending track 47, the mean RMSE goes from 8.78 to 6.38 mm, representing a 27.3% noise reduction (Table S2 in Supporting Information S1).

After the long-wavelength error correction, the two tracks of InSAR time series data are used to derive the line-of-sight (LOS) velocity fields through least squares regression. The InSAR LOS velocity fields are referenced to the Eurasian-fixed reference frame, by minimizing the post-fit residuals between the InSAR-observed and GPS-projected LOS velocities at CGPS sites, whose 3-D velocities are referenced to the Eurasian-fixed reference frame. Given the region's predominant horizontal tectonic movement (Xu & Ji, 2015) and no major earthquakes during this study's timeframe (https://earthquake.usgs.gov/), a steady-state horizontal deformation field with a constant deformation rate is assumed, which is represented by the horizontal GPS velocity field (Figure 2a). With GPS-provided constraints for the horizontal deformation, we perform a weighted least squares inversion to convert the InSAR mean LOS velocity and displacement time series data for the two tracks (Figures 2b and 2c) into the vertical velocity field and time series (Figure 2d). We also employ a bootstrap method provided by StaMPS (Hooper et al., 2007) to estimate the uncertainties of the InSAR mean LOS velocities (Figures S8a and S8b in Supporting Information S1), which are subsequently converted to uncertainties of the vertical mean velocities (Figure S8c in Supporting Information S1). Details of this procedure can be found in the Text S1 in Supporting Information S1.

4.2. Seasonal and Long-Term Pattern Extraction

We use a sinusoidal function to model the annual variation of deformation, and a quadratic polynomial for long-term deformation. The annual deformation signal is considered elastic and recoverable, while the long-term

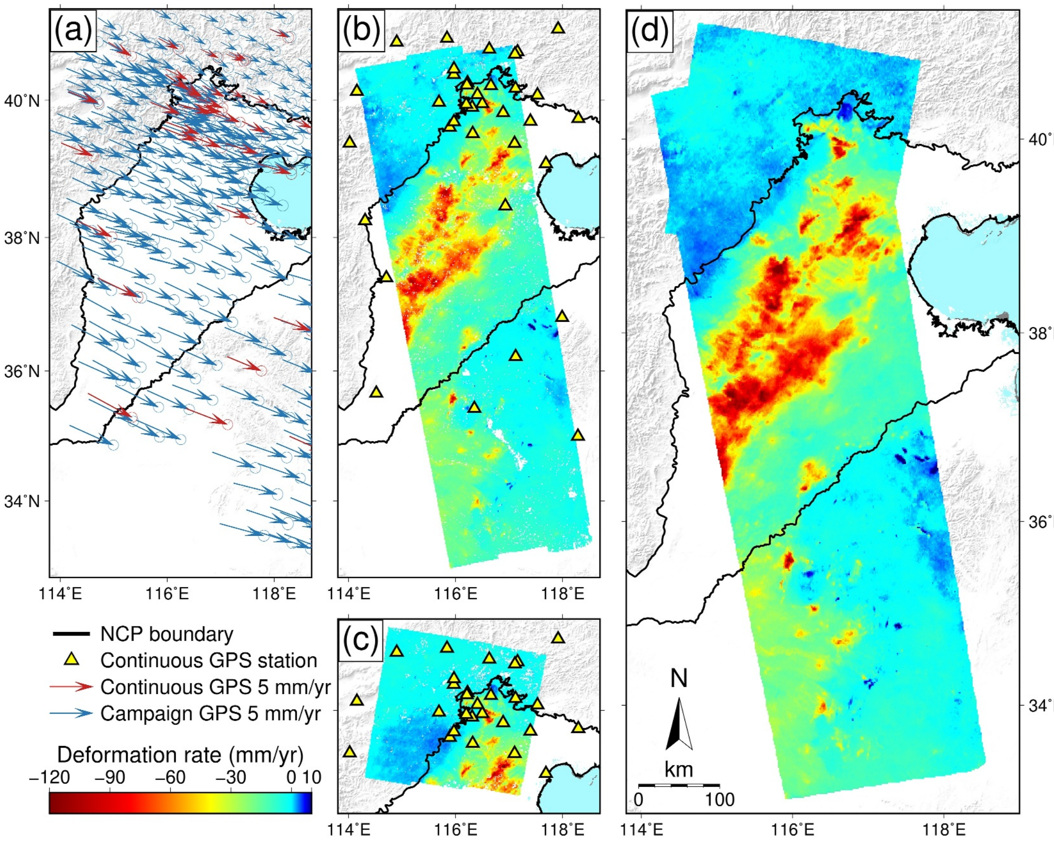

Figure 2. (a) Horizontal GPS velocity field in NCP with respect to the Eurasia plate. The red and blue arrows denote the velocities of the CGPS and campaign GPS sites respectively. (b, c) InSAR mean LOS velocities for ascending track 142 and descending track 47 respectively, where all the points in both tracks are PS pixels. (d) Derived vertical velocities in NCP. The yellow triangles are CGPS stations, and black lines mark the boundary of NCP.

deformation is mostly elastic but may also have an inelastic component which is unrecoverable (Poland & Ireland, 1988; Wilson & Gorelick, 1996). Accordingly, the fitting formula is:

$$D(t) = B\sin(2\pi t) + C\cos(2\pi t) + K_0 + K_1 t + K_2 t^2 \tag{1}$$

where t is time with the unit of year, $D(t)$ is the surface vertical deformation, and B, C, K_0, K_1, and K_2 are the fitting coefficients. K_0, K_1, and K_2 are the fitting coefficients of the constant, linear, and quadratic terms, respectively.

Accordingly, the seasonal deformation component (which is recoverable and elastic) can also be described as:

$$D_{\text{seasonal}}(t) = B\sin(2\pi t) + C\cos(2\pi t) = A_D \times \cos\left(2\pi t - \varphi_D\right) \tag{2}$$

where A_D and φ_D are the amplitude and phase of the seasonal deformation. The long-term deformation component is described as:

$$D_{\text{long-term}}(t) = K_0 + K_1 t + K_2 t^2 \tag{3}$$

where K_0 serves as the reference for deformation and does not have practical physical meaning. K_1 and K_2 represent the long-term deformation rate and its acceleration, respectively. The long-term deformation is considered mostly elastic if the hydraulic head did not fall below historical lows (Wilson & Gorelick, 1996)—a condition which was met in most of the NCP 2015–2019 (Yang et al., 2021).

We use F-test for regression analysis (Anderson & Conder, 2011; Shen et al., 1996; St & Wold, 1989) to determine whether a more complex model with additional parameter(s) outperforms a simpler model in capturing observational data with statistical confidence. The F statistic is defined as:

$$F = \left(\frac{\mathrm{RSS}_1 - \mathrm{RSS}_2}{k_2 - k_1}\right) \Big/ \left(\frac{\mathrm{RSS}_2}{n - k_2}\right) \tag{4}$$

where RSS denotes the sum squares of residuals between observations and predictions, k is the number of model free parameters, and n is the number of observations. Subscripts 1 and 2 represent the simple and complex models, respectively. A more detailed explanation of this method can be found in the Text S2 in Supporting Information S1.

For the hydraulic head data, based on the mechanism of hydraulic head changes, we exclude the quadratic term and use only seasonal and linear terms in the fitting function:

$$H(t) = B' \sin(2\pi t) + C' \cos(2\pi t) + K_0' + K_1' t = A_H \times \cos\left(2\pi t - \varphi_H\right) + K_0' + K_1' t \tag{5}$$

where t is time with the unit of year, A_H represents the hydraulic head's magnitude, while φ_H indicates its peak time. K_0' and K_1' are the fitting coefficients for the constant and linear terms, respectively. However, given the relatively short data span for most hydraulic head observations (from the National Groundwater Monitoring Center of China, observed from January 2018 to December 2019), we disregard the linear trend and focus on seasonal hydraulic head variations, which are primarily associated with elastic deformation in NCP.

4.3. Aquifer Physical Property Estimation

In hydrology, storativity S is a pivotal and dimensionless aquifer parameter, which indicates the aquifer's ability to retain or release groundwater. This term indicates the volume of fluid discharged from the total porous medium per unit surface area of the aquifer for each unit change in hydraulic head (Freeze & Cherry, 1979). In a laterally extended aquifer, assuming that the compressibility of water is negligible, the storativity can be represented as:

$$S = -\rho g \frac{\Delta b}{\Delta \sigma_e} \tag{6}$$

where ρ is the density of water [kg/m^3], g is the gravity acceleration 9.8 m/s^2, and Δb is the variation in aquifer thickness [m] due to the changes in effective stress $\Delta\sigma_e$, and positive Δb means uplift. The effective stress is defined as: $\sigma_e = \sigma_t - p$, where σ_t is the total loading stress and p is the pore pressure (Terzaghi, 1925) (Figure 3).

We estimate aquifer storativity under two different scenarios. For the first scenario, we disregard the contribution of geostatic loading change in the unconfined aquifer, focusing only on hydraulic head changes in the confined aquifer. Under this scenario, the overburden of the aquifer remains constant, and the change of the effective stress is $\Delta\sigma_e = -\Delta p$. Accordingly, the storativity is:

$$S_0 = \frac{\Delta b}{\Delta h_c} \tag{7}$$

where Δh_c is the water head change in the confined aquifer [m]. Here, positive Δh_c means a water level increase, and Δb equals to the elastic vertical surface deformation observed by InSAR.

For the second scenario, we account for geostatic loading change due to the water level changes in the unconfined aquifer, which changes the overburden on the confined aquifer and the pore pressure in the confined aquifer (Leake & Galloway, 2007; Poland & Davis, 1969). The geostatic loading change due to the change of water level in the unconfined aquifer is $\sigma_t = \rho g n \Delta h_u$, where n is the porosity of the unconfined aquifer and Δh_u is the change of water level in the unconfined aquifer. Here, we ignore the water content change due to the change of moisture contained above the water table. The pore pressure change in the confined aquifer is $\Delta p = \rho g \Delta h_c$. Therefore, the change of effective stress in the confined aquifer is $\Delta\sigma_e = \rho g(n\Delta h_u - \Delta h_c)$. Consequently, the storativity is expressed as:

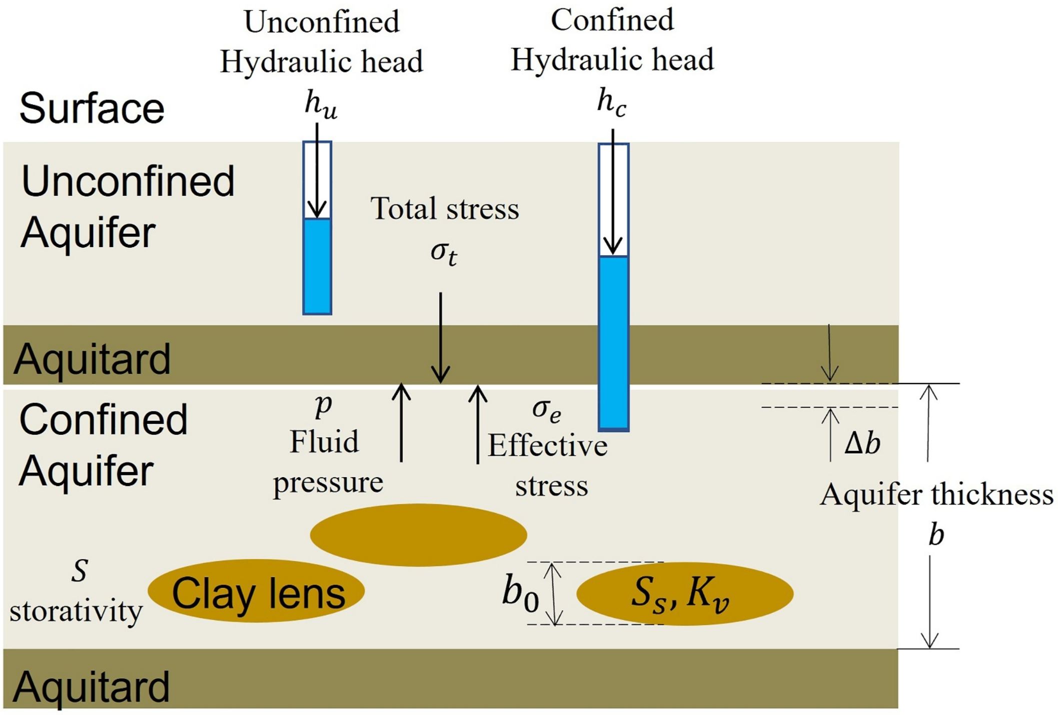

Figure 3. A theoretical framework of aquifer deformation system, modified from Chen et al. (2016). The model comprises permeable aquifers and relatively impermeable aquitards. There are embedded thin clay units known as clay lenses in the confined aquifer, which consist of clay with low hydraulic conductivity, and are surrounded by sand with high hydraulic conductivity. The physical terms are: thickness b_0, specific storativity S_s and vertical hydraulic conductivity K_v for clay lenses, storativity S, thickness b and its change Δb for confined aquifer. The physical observables are: unconfined hydraulic head h_u and confined hydraulic head h_c.

$$S_1 = \frac{\Delta b}{\Delta h_c - n\Delta h_u} \tag{8}$$

Overall, the storativity of aquifer can be well assessed by combining the surface deformation and the observation of water level change in the confined and unconfined aquifer (Figure S9 in Supporting Information S1). Here we ignore the deformation caused by the groundwater loading effect due to its negligible contribution (Li et al., 2022).

There is typically a time delay between the hydraulic head change and the corresponding surface elastic displacement, as different parts of the aquifer require time to equilibrate to the changing stress. Confined aquifers usually contain sand with high hydraulic conductivity and embedded thin clay lens with low hydraulic conductivity (Figure 3). Sandy portions response simultaneously, producing in-phase elastic deformation with water head change. In contrast, clay lenses, due to their low hydraulic conductivity, need time to equilibrate. This process can be represented as one dimensional diffusion process (Chen et al., 2016; Riley, 1970; Rousseau-Gueutin et al., 2013), with the associated delay time τ_H, represented as:

$$\tau_H = \left(\frac{b_0}{2}\right)^2 \frac{S_s}{K_v} \tag{9}$$

where b_0 is the clay lens thickness, S_s is the specific storativity of the clay lenses, and K_v is the vertical hydraulic conductivity of the clay lenses, respectively.

The delay time between seasonal deformation data and seasonal varied water head is calculated using the following equation:

$$\tau_H = \left[(\varphi_D - \varphi_H) \ \% \ 2\pi \right] \times \frac{365}{2\pi} \tag{10}$$

where τ_H is the delay time in days, φ_D is the phase of seasonal deformation and φ_H is the phase of hydraulic head; % denotes the modulo operation on 2π (assuming τ_H is no more than 1 year) to ensure positive values for causality in the hydrological process.

4.4. GWS Change Estimation

Based on the definition of storativity S in the confined aquifer, we can calculate the GWS change in the confined aquifer over the observation time as:

$$V_c = \int_A S * \Delta h_c \, da \tag{11}$$

where a is the area and Δh_c is the water level change in the confined aquifer during the study period. For calculations excluding contribution from geostatic loading change, we use storativity S_0; when including contribution from geostatic loading change, we use S_1.

The GWS change in the unconfined aquifer can be calculated as:

$$V_u = \int_A n * \Delta h_u \, da \tag{12}$$

where n is the porosity and Δh_u is the water level change in the unconfined aquifer during the study period. Whereas, contribution due to changes in the moisture content above the water table is ignore.

5. Results and Analysis

5.1. Surface Deformation in NCP

We integrate GNSS and InSAR data, and derive the mean vertical deformation velocities in the NCP between 2015 and 2019 (Figure 4a). The surface deformation in NCP derived from geodetic measurements is dominated by vertical land subsidence resulting mainly from anthropogenic activities, with an average subsidence rate of ~29 mm/yr (Figure 4a), rather than tectonically related horizontal motion (Figure 2a). Notably, the densely-populated central NCP exhibits significant and widespread subsidence with rates up to 120 mm/yr due to excessive groundwater extraction for agriculture irrigation (Y. Zhang et al., 2020) (Figure 4a). This is consistent with previous findings (Shi et al., 2020; Zhao et al., 2017). Uncertainties for vertical mean velocities remain within 4 mm/yr (Figure S8c in Supporting Information S1). On the other hand, mountainous regions located outside of NCP, to the southeast and northwest, exhibit minor and broadly dispersed uplifts around 2~3 mm/yr (Figure 4a), which may be associated with mass unloading due to long-term groundwater extraction, analogous to findings from central California (Amos et al., 2014). For this study, our primary focus lies on the hydrological-induced deformation within the NCP.

A noticeable gradient in subsidence rates is evident along the provincial boundary between Hebei and Shandong Provinces (Figure 4a). This correlation is more significant than other correlations such as those with faults and/or geomorphology (Figures 4c and 4d), particularly regarding the large-scale deformation pattern. We think this gradient is related to local water usage. The record of annual groundwater supply indicates that Shandong Province consumed less groundwater than Hebei Province over the last decade (Figure 4b), resulting to significantly less subsidence in Shandong (approximately −20 mm/yr), than that in Hebei (approximately −80 mm/yr). This observation suggests that regional policy differences in groundwater extraction critically influenced the spatial distribution of subsidence.

The effect of active fault zones on hydrological-induced deformation remains to be complex. Notably, we observe a uniform and smooth deformation pattern across the THCFS in southern NCP (Figures 4c and 4d), but divergent deformation patterns across other faults in northern NCP (Figure 4e). The variations of observed uplift rates

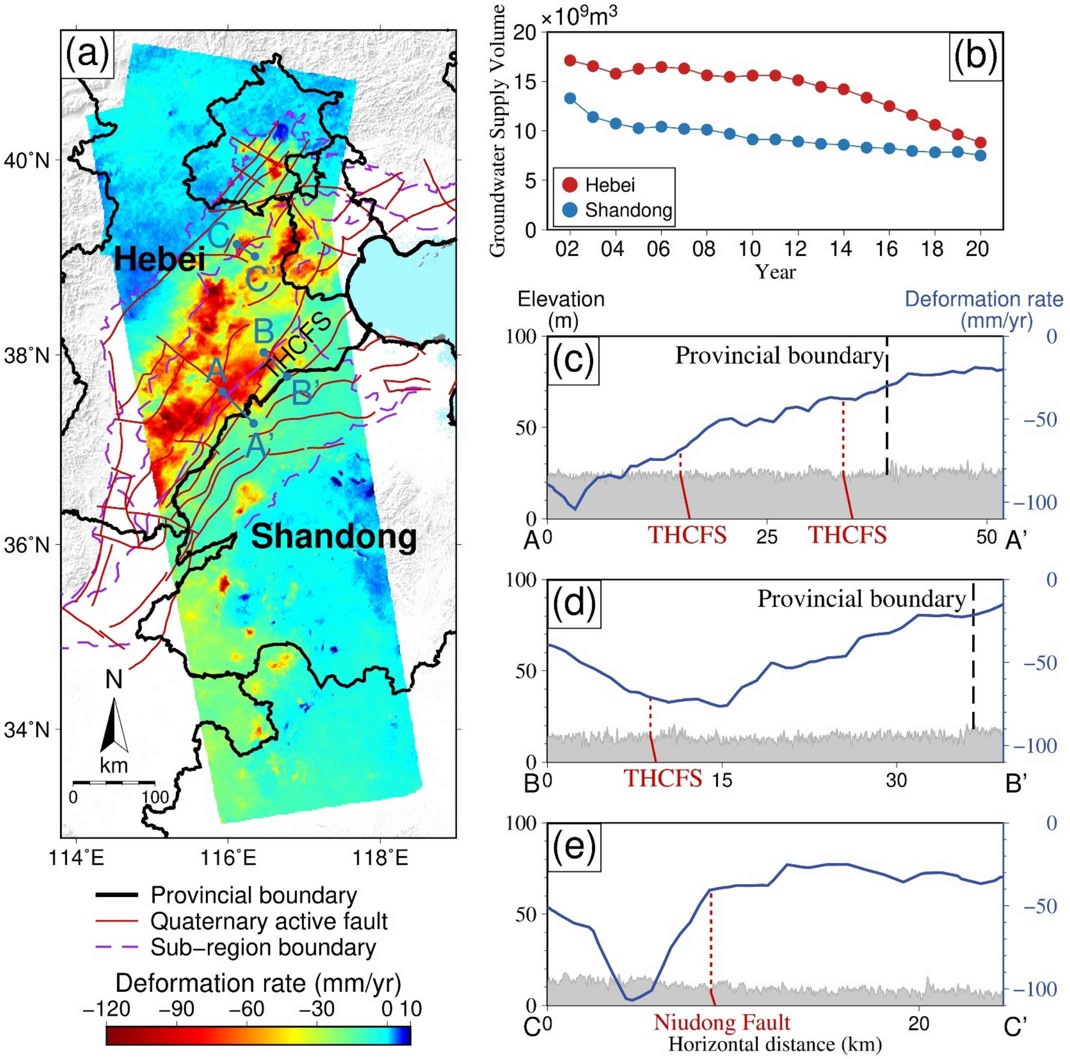

Figure 4. (a) Vertical deformation velocities in NCP. Red lines represent quaternary active faults (Deng, 2003). Black lines delineate the provincial borders and blue lines mark the profiles (AA′, BB′, CC′). Purple dashed lines represent the NCP boundary. (b) Annual groundwater supply statistics for Hebei and Shandong Provinces, covering the period from 2002 to 2020 (http://www.stats.gov.cn/sj/ndsj/). (c–e) show vertical deformation rates and elevation along the AA′, BB′, and CC′ profiles, respectively.

across some faults in the northern NCP can be attributed to the difference in fault material's hydraulic conductivity. High clay content within the fault core results in low hydraulic conductivity, creating a barrier to cross-fault fluid flow (Bense et al., 2003; Chaussard et al., 2014, 2017). However, the THCFS in the southern NCP does not function as hydraulic barriers, possibly due to differences in fault structure.

5.2. Seasonal and Long-Term Deformation Patterns in NCP

The seasonal deformation exhibits remarkable spatial variation (Figures 5a and 5b). The amplitude A_D in the central plain area markedly exceeds that in surrounding regions, averaging 8 mm and peaking at approximately 25 mm within the HRP (Figure 5a). The average amplitude of seasonal deformation in PP and YRP is 5 ~ 6 mm. The time epoch to achieve the peak of the seasonal deformation φ_D in a year is also different across the whole NCP. The peak annual change of HRP occurs around March and April, while that of YRP is around July and August. The spatial distribution of phase of annual deformation demonstrates a coherent spatial pattern associated with the groundwater sub-regions, manifesting notable phase disparity between the HRP and the YRP (Figure 5b).

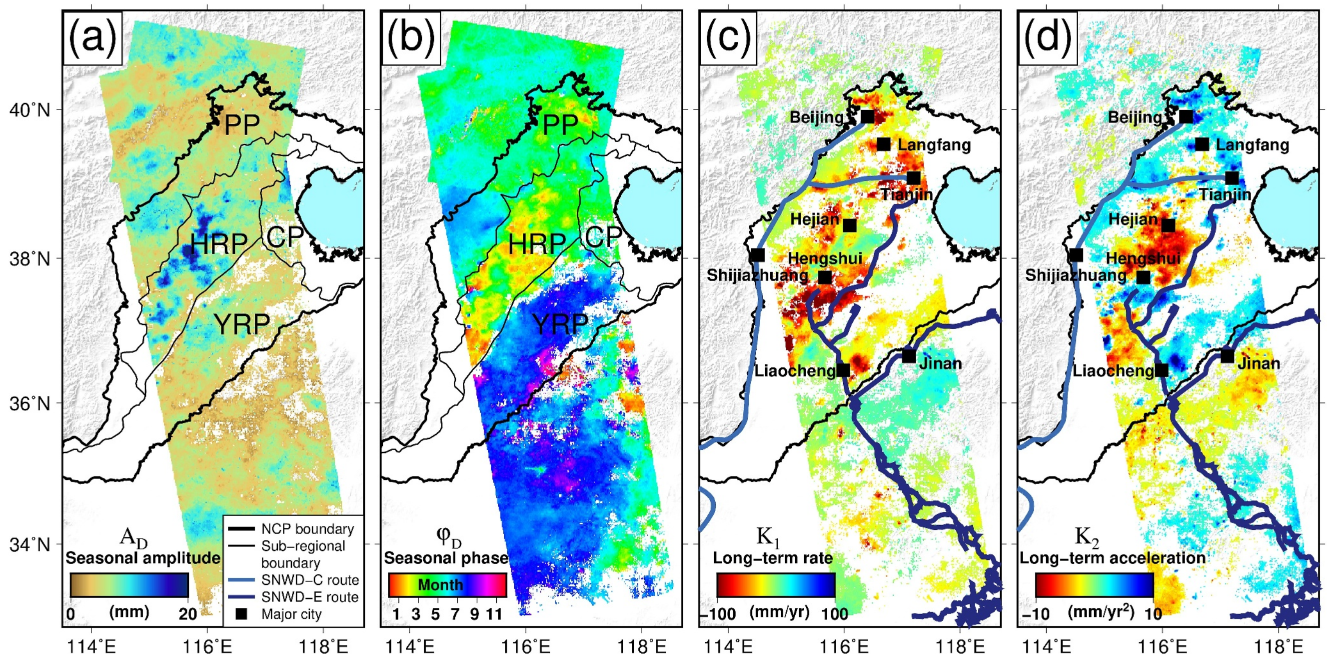

Figure 5. Seasonal and long-term vertical deformation pattern in NCP. (a, b) illustrate amplitude A_D and phase φ_D of seasonal deformation for pixels with 95% confidence from F-test, respectively. (c, d) present spatial distribution of linear (K_1) and quadratic (K_2) term coefficients of long-term deformation for pixels with 95% confidence from F-test, respectively.

The long-term deformation is composed of two terms: the linear deformation rate (K_1) and the acceleration of the deformation rate (K_2). The long-term deformation rate reveals widespread subsidence within the NCP, with a maximum subsidence rate at 100 mm/yr, while minor uplift areas appear externally (Figure 5c). Meanwhile, the long-term deformation acceleration during 2015–2019 spans from -10 mm/yr^2 to 10 mm/yr^2, indicating a changing trend of existing long-term subsidence in NCP (Figure 5d). Here we use F-test method to test statistical significance of the deformation components. The first test compares two models, one incorporates the linear long-term deformation only and the other includes both the linear long-term and seasonal (sinusoidal) deformation. The F-test result shows that inclusion of the seasonal term exceeds 95% confidence level at about 85.2% of the region in NCP and the surrounding area (Figures 5a and 5b; Figure S10a in Supporting Information S1). The second test compares two models, one incorporates the seasonal and linear long-term deformation, and the other comprises the quadratic (acceleration) deformation in addition to all the terms in the first model. The test result illustrates that the quadratic long-term deformation (K_2) is significant at the 95% confidence level in about 40.2% of the region in NCP and the surrounding area, mostly within NCP (Figures 5c and 5d; Figure S10b in Supporting Information S1).

The spatial variation of long-term acceleration shows a very interesting pattern (Figure 5d). Specifically, areas with a positive K_2, denoting subsidence deceleration, predominantly along the SNWD Project aqueduct lines and around major cities such as Beijing, Tianjin and Liaocheng City (Figure 5d). This alignment underscores the significant role of water diversion from the SNWD Project in groundwater replenishment and effective subsidence deceleration in these urban areas. Contrastingly, areas like Hejian City (Figure 5d), situated away from the SNWD aqueduct lines, exhibit a negative K_2, signaling ongoing subsidence acceleration due to limited groundwater replenishment from the SNWD Project.

5.3. Seasonal Variation of Hydraulic Head

The amplitude and phase of the hydraulic head's seasonal variation also exhibit pronounced spatial patterns. The amplitude variation is notably larger in the HRP compared to other groundwater sub-regions in NCP, peaking around at 10 m (Figure 6a). Meanwhile, in the YRP, the amplitude peaks at around 3 m, highlighting a spatial difference between the two sub-regions (Figure 6a). Regarding the phase, its variation demonstrates a high spatial

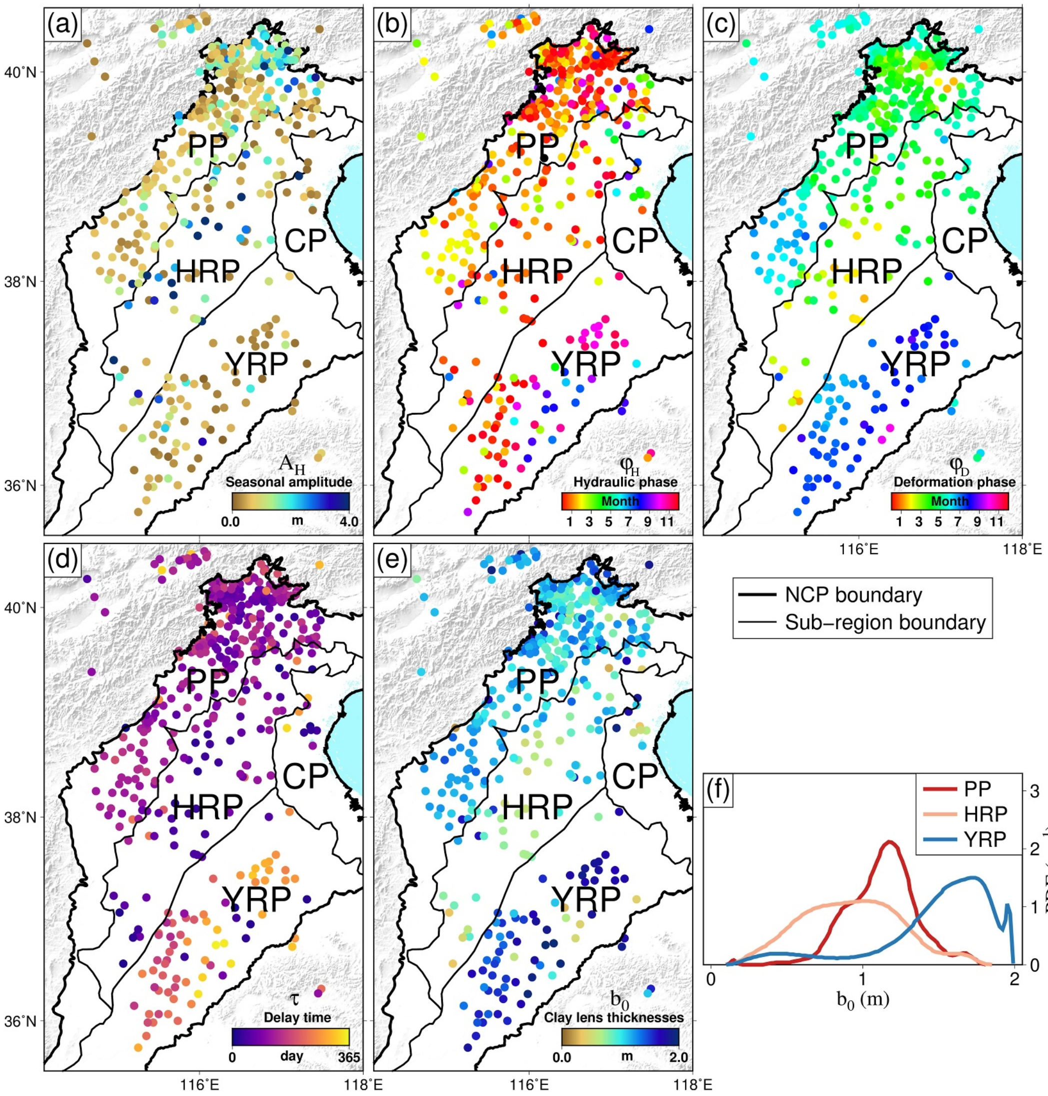

Figure 6. Phase delay time and clay lens thickness estimates. (a) Illustrates the amplitude A_H of hydraulic head. (b, c) demonstrate phase φ_H of hydraulic head and phase of seasonal deformation φ_D. (d, e) illustrate the spatial distribution of derived delay time τ_H and clay lens thicknesses b_0. (f) Shows the probability density function (PDF) of b_0.

correlation with the partition of groundwater sub-regions in NCP, with greater phase in the south than in the north of NCP (Figure 6b).

5.4. Aquifer Physical Properties

5.4.1. Clay Lens Thickness

The thickness of clay lens can affect the phase lag (Figure 6d) of surface deformation (Figure 6c) behind the hydraulic head change (Figure 6b). Assuming a homogeneous vertical hydraulic conductivity K_v of 9×10^{-6}m/d and a homogeneous specific storativity S_s of $3.3 \times 10^{-3}\ \mathrm{m}^{-1}$ for the clay lenses (Daniel, 1989; Grisak & Cherry, 1975), the estimated clay lens thicknesses in NCP (Equation 9) ranges from 0.15 to 1.98 m (Figure 6e), with an average of 1.13 m for PP, 0.92 m for HRP and 1.48 m for YRP, respectively. The probability density function (PDF) of clay lens thicknesses b_0 across three sub-regions (Figure 6f) shows distinct spatial variations, with the highest values in the YRP, the lowest in the HRP, and moderate levels in the PP.

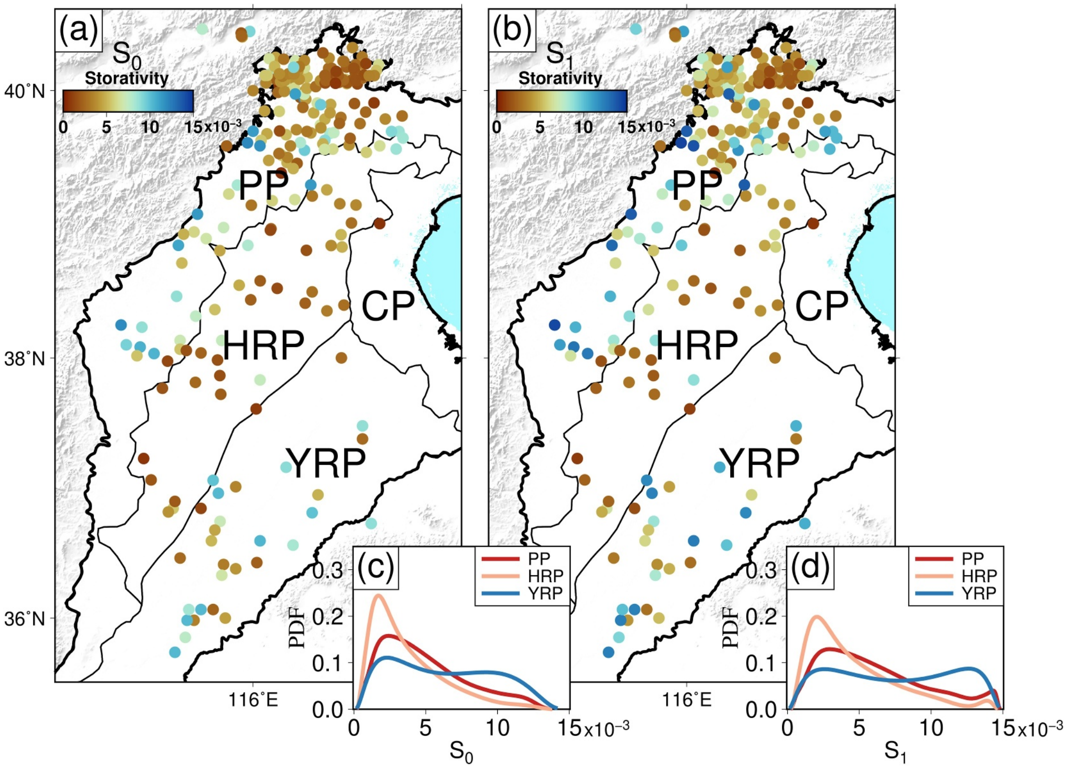

Figure 7. Spatial distribution of aquifer physical properties in NCP and corresponding PDF within three groundwater sub-regions. (a, b) illustrate the storativity S_0 and S_1, while (c, d) present corresponding storativity PDF of (a, b).

5.4.2. Storativity

Without accounting for geostatic loading change, all the observed seasonal deformation is caused by the seasonal variation of water head in the confined aquifer. The corresponding storativity S_0 values at 243 wells in NCP can be estimated by the ratio between the amplitudes of seasonal deformation and seasonal hydraulic head change (Equation 7), resulting in a range of 0.55×10^{-3}–11.94×10^{-3} (Figure 7a). Outliers are removed to ensure the reliability of these values, corroborated by findings in related hydraulic research (Zhang, Fei, et al., 2009). When accounting for geostatic loading change, the storativity S_1 can only be estimated at 46 observation sites that monitor both confined and unconfined aquifers (Equation 8). Utilizing a porosity value of 0.21 for the unconfined aquifer, as estimated from sediment layers in NCP (Li et al., 2011), the calculated S_1 values range from 0.87×10^{-3} to 15.72×10^{-3} across the 46 sites (Table S3 in Supporting Information S1).

We compare storativity estimates under two scenarios across 46 sites to quantitatively assess the impact of the unconfined aquifer. Estimates with and without accounting for geostatic loading change differ significantly, with the former being on average 20.4% greater than the latter. This result is consistent with a 23% increase reported by Li et al. (2022) using geodetic and hydrological data at the Huairou Groundwater Reserve Site, located near the northern boundary of the NCP. Consequently, assuming the same ratio between the results of accounting and not accounting for geostatic loading change, we can calculate the S_1 values at all 243 wells, with the results ranging from 0.67×10^{-3} to 14.38×10^{-3} (Figure 7b). As detailed in Text S3 and Table S3 in Supporting Information S1, uncertainties of the storativity estimates are usually significantly smaller than the storativity estimate values.

The PDFs of storativity highlight significant spatial variation across the NCP, peaking in the YRP and dipping to its lowest in the HRP for both S_0 and S_1 (Figures 7c and 7d). The spatial distributions of clay lens thickness and storativity align with the groundwater sub-regions divisions, suggesting a link to the formation of sedimentary units through geological history.

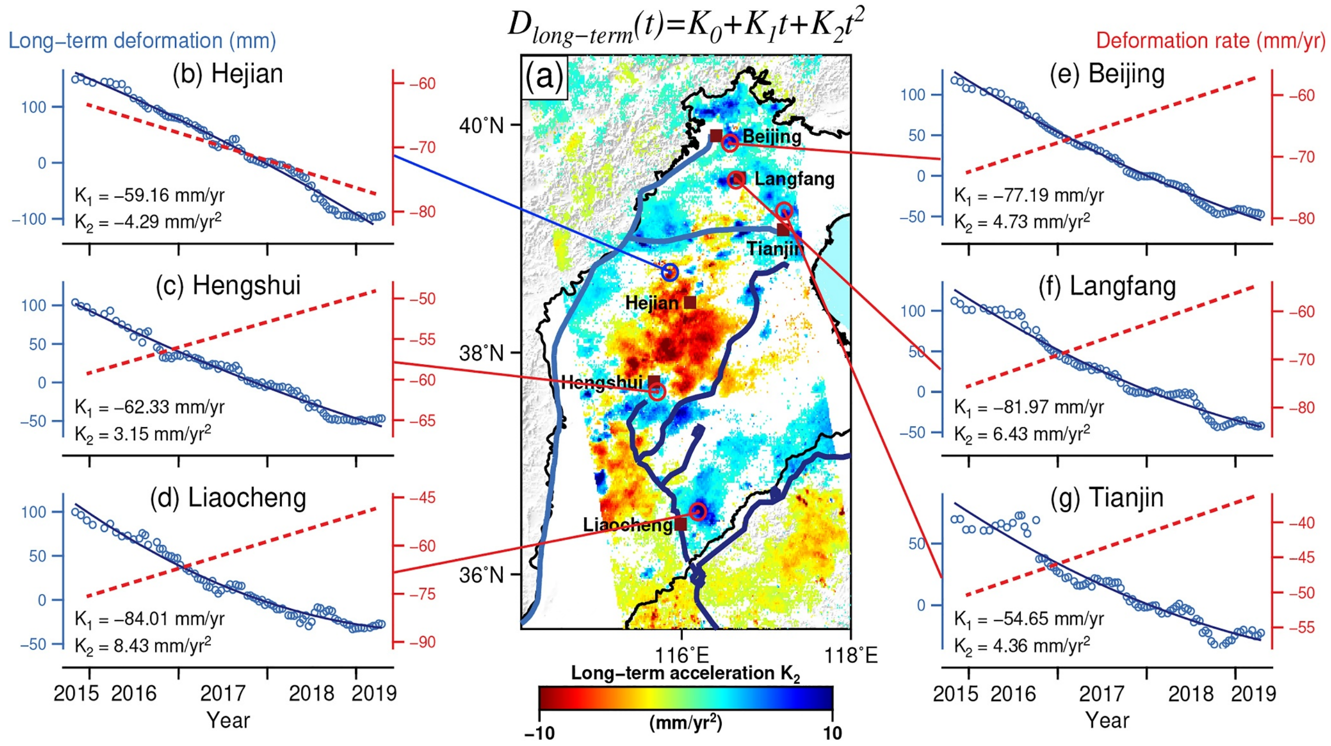

Figure 8. Cumulative long-term deformation and extracted deformation rate around selected cities. (a) Presents spatial distribution of quadratic term (K_2) of long-term deformation. Panels (b) denotes deformation change at Hejian City, characterized by a negative acceleration term ($K_2 < 0$), while panels (c–g) represent cities with a positive acceleration term ($K_2 > 0$). Blue circles denote the observed long-term deformation, and the dark blue lines represent the model fitting of the data. The red dashed lines depict the corresponding deformation rate incorporating both linear and quadratic terms, calculated as the first-order derivative of the long-term deformation function.

5.5. GWS Change in NCP

GWS change in confined aquifer can be calculated using storativity and hydraulic head change within the aquifer (Equation 11), which is closely related to the high-resolution deformation observations. By integrating the subsidence rate (K_1) and the acceleration term (K_2) over the observation time span, we can obtain an average accumulated subsidence of 115.6 mm over 4 years across NCP. Without accounting for geostatic loading changes, the average GWS depletion rate in the confined aquifer is at 28.9 mm/yr per unit area for the whole region, assuming elastic long-term deformation. When considering geostatic loading change, the average GWS depletion rate is 34.8 mm/yr per unit area. Furthermore, some regions with dense well observations enable precise GWS change assessments, such as declines of 5.6 mm/yr for Beijing and 30.1 mm/yr for Tianjin per unit area without considering geostatic loading change, while 6.8 mm/yr for Beijing and 36.3 mm/yr for Tianjin by considering geostatic loading change.

Estimation of GWS change in the unconfined aquifer is limited by the availability of long-term hydraulic head observations for unconfined aquifer wells across the NCP, so we can only provide an estimate based on the spatial interpolation and extrapolation of water level changes in the unconfined aquifer. Using this estimation (Equation 12), the average depletion rate is 16.5 mm/yr per unit area in the unconfined aquifer. However, the denser distribution of unconfined aquifer wells in Beijing and Tianjin allows for more reliable estimates, which indicate localized recovery. Specifically, Beijing shows a slight recharge rate of 0.8 mm/yr per unit area, while Tianjin exhibits a higher recharge rate of 4.7 mm/yr per unit area.

Additionally, the impact of SNWD project on GWS changes can be estimated by analyzing the acceleration term K_2 (Figure 8a). This term reflects the rate of change in deformation rate, influenced by both natural processes and human activities, such as water diversion and groundwater extraction (Zhao et al., 2019). The deformation due to acceleration term is defined as $D_{\text{Acceleration}} = K_2\, t^2$, which can be used to estimate GWS change (Equation 11). In this analysis, we focus on six major cities in NCP to represent GWS change across the region. Areas with negative acceleration ($K_2 < 0$), which may not have benefited from the SNWD Project such as Hejian City, account for a

GWS reduction of 1.03 km^3 over the 4-year period, corresponding to a rate of 0.26 km^3/yr (Figure 8b). In contrast, regions with positive acceleration ($K_2 > 0$) have experienced effective recharge likely due to the SNWD project, primarily along the project's aqueduct lines (Figures 8c–8g), which cover 55% of the NCP region studied. These regions show an GWS increase of 1.02 km^3 over the 4-year period, corresponding to a rate of 0.25 km^3/yr. Although the Central Route of the SNWD Project diverts 9.5 km^3/yr of water (Long et al., 2020), most of this water is used for industrial and agricultural purposes, with only a small fraction contributing to aquifer recharge. This allocation underscores the limited direct impact on groundwater recharge, despite the significant volume of water diverted. The strong correlation between regions of positive acceleration and the SNWD project's aqueduct lines further validates the project's positive impact on GWS in these areas. Overall, the observed slowdown in subsidence and reduction in GWS depletion across the NCP confirm that, although the large-scale subsidence is still occurring, the trend has slowed in certain areas, particularly in major cities along the routes of the SNWD Project.

6. Discussion

6.1. Assessment of Aquifer Physical Property Estimates

The aquifer properties derived from our study align with prior studies in the alluvial plain aquifers of the NCP. For example, our storativity estimates range from 0.67×10^{-3} to 14.38×10^{-3}, which are consistent with estimates of 1×10^{-3} to 8×10^{-3} reported by Cao et al. (2013) and Zhang, Fei, et al. (2009). Additionally, Jiang et al. (2018) reported the storativity pattern of the Cangzhou aquifer system in the central NCP, with values ranging from 1.7×10^{-4} to 4.4×10^{-3}, which also agrees with our results. Our analysis, however, provides the most comprehensive results, offering better spatial coverage and captures sub-regional characteristics, based on effective data acquisition across large regions.

Our investigation also provides estimates of the clay lens thickness in the NCP, ranging from 0.15 to 1.98 m. As no previous studies on the physical properties of clay lenses are available for the NCP region, we compare our result with those from other regions worldwide. For instance, Chen et al. (2016) reported a delay time of 25–65 days at six wells in Colorado's San Luis Valley; while our study, which incorporates more observational data distributed across various locations in the NCP, shows a mean delay time of 134 days across 472 observation sites (Figure 6d), suggesting a thicker average clay lens in the NCP. This difference may arise from differences in depositional environments: the San Luis Valley is a high-elevation depositional basin, whereas the NCP is a large alluvial plain formed by long-term river deposition (Zhang, Fei, et al., 2009), which may account for this variation.

Comparing the spatial distribution of clay lens thicknesses b_0 (Figure 6e) and storativity S_0 and S_1 (Figures 7a and 7b) with the division of groundwater sub-regions in NCP, a significant divergence in the aquifer physical properties emerges across groundwater sub-regions. Key observations include the follows:

The northwestern PP has the moderate storativity distribution compared with other sub-regions. The clay lenses here are about 0.8–1.3 m thick, thicker than the HRP but thinner than the YRP. The abundance of coarse-grained aquifers in the PP likely contributes to its moderate storativity. Conversely, the vicinity around the northern Beijing Plain shows diminished storativity and thinner clay lenses, which is possibly attributed to the area's flat terrain, which amplifies the deposition effect, refining aquifer grain and decreasing storativity.

Located in the southern NCP region, the YRP has highest storativity and the thickest clay lenses in the region, ranging 1.3–2.0 m. Historic flooding by the ancient Yellow River is believed to have resulted in significant sedimentation, producing these considerably thicker clay lenses.

Characterized by minimal storativity and thin clay lenses (0.5–1.0 m), the central HRP's features are attributed to the prolonged stream erosion by the Hai River and its upstream tributaries, but without substantial sedimentation. The aquifers here, composed of fine grains and thin clay lenses, result in lower storativity compared to both the northwestern PP and the southern YRP.

6.2. Comparison of GWS Change Results

GWS change can be measured using diverse data types, each uncovering unique aspects of these changes. Our approach, based on high spatial resolution geodetic data, captures the spatial variation patterns of GWS change,

Table 1

Comparison of GWS Change Estimates Across Different Research Areas and Data Types

					GWS change in our study		
Research source	Research area	Research period	Data type	GWS change from previous research	Confined aquifer (No geostatic loading)	Confined aquifer (with geostatic loading)	Unconfined aquifer
Liu et al. (2022)	NCP	2015–2022	GRACE	−27.6 ± 5.5 mm/yr	−28.9 mm/yr	−34.8 mm/yr	−16.5 mm/yr
Zhang et al. (2023)	NCP	2015–2022	GRACE	−22.6 mm/y	−28.9 mm/yr	−34.8 mm/yr	−16.5 mm/yr
C. Zhang et al. (2020)	NCP	2015–2018	unconfined well data	0.3 km^3/yr	−2.62 km^3/yr	−3.15 km^3/yr	−1.49 km^3/yr
Long et al. (2020)	Beijing	2006–2018	hydrologic model	−8.5 mm/yr	−5.6 mm/yr	−6.8 mm/yr	0.8 mm/yr
Su et al. (2023)	Tianjin	2015–2019	InSAR & GNSS	−24.3 ± 0.2 mm/yr	−30.1 mm/y	−36.3 mm/y	4.7 mm/yr

details that other sources may overlook. The significant spatial disparity in subsidence patterns across the NCP highlights our method's precision in identifying local GWS changes (Figure S11 in Supporting Information S1). We compile and compare results from multiple sources with our findings in Table 1 and investigate possible causes of their differences.

As Table 1 shows, our estimates of GWS change in confined aquifer under two scenarios are generally consistent with previous research, although differences are noticeable. One of the causes may come from the challenge of distinguishing between elastic and inelastic components from the long-term deformation, potentially leading to biased estimates of GWS change in confined aquifer calculations. Besides, as mentioned in Section 5.4.2, the effect of geostatic loading change in the unconfined aquifer, contributing 20.4% of the total storativity, is not predominant in the estimation of GWS change. For our estimates of GWS change in the unconfined aquifer, the accuracy is limited due to the sparse distribution of observation wells, and the rough estimates of porosity, particularly for the whole NCP (Figure S11c in Supporting Information S1). However, the results for Beijing and Tianjin are relatively more reliable due to the higher density of observation wells. Additionally, Su et al. (2023) reported a GWS depletion rate of −24.3 ± 0.2 mm/yr for Tianjin, a result that significantly differs from our value of −31.9 mm/yr (calculated by adding the confined aquifer with geostatic loading value and the unconfined aquifer value). This discrepancy is due to our analysis being limited by the scope of geodetic measurements and focusing solely on the western region of Tianjin, where subsidence is most severe.

Intriguingly, C. Zhang et al. (2020) reported an unexpected GWS increase of +0.3 km^3/yr in the NCP during 2015–2018, based only on unconfined well data, while our analysis yields a GWS decline. Assuming a study area of 9.1×10^4 km^2, our study estimates the confined GWS depletion rates as −2.62 km^3/yr without geostatic loading change and −3.15 km^3/yr with geostatic loading change. This discrepancy might arise from the uneven distribution of 559 unconfined wells in C. Zhang et al.'s study, predominantly lacking data from NCP's central region where GWS depletion is most severe. Additionally, GWS changes are primarily influenced by the deeper confined aquifers, which are not reflected in measurements from only shallow unconfined aquifers. In summary, our geodesy-based method more effectively captures precise and continuous spatial changes of GWS in the NCP.

6.3. Effect of Groundwater Use Management on Land Subsidence

Land subsidence can result from natural causes, such as tectonic movement and changes in precipitation, as well as from anthropogenic causes. In NCP, the extensive groundwater extraction stands as the predominant cause of its subsidence. Therefore, the enactment and implementation of groundwater use regulations in different administrative regions may lead to observed spatial disparities in subsidence patterns.

The Hebei and Shandong Provinces bear considerable similarities, each hosting substantial human populations (~75 million for Hebei and ~100 million for Shandong, http://www.stats.gov.cn/sj/ndsj/) and predominantly agricultural economies. Despite these similarities, their approaches to groundwater management diverged markedly over the last couple of decades. Shandong Province, as per available statistics, has rigorously regulated groundwater exploitation, leading to a consistent reduction in groundwater extraction each year since 2003 (http://asianlii.org/chi/cn/legis/sd/laws/74b2a59508e71c356466fe051a23c60fdb61e62f/). In contrast, Hebei Province's extensive groundwater extraction persisted till 2013 when the Chinese central government intervened (http://www.gov.cn/zwgk/2013-01/06/content_2305762.htm). The ten-year-long disparity in groundwater use regulation and implementation (Figure 4b) has led to significant differences in deformation characteristics between the two provinces. This has resulted in widespread subsidence across Hebei Province, while Shandong Province has not experienced large-scale subsidence. Figure 4a starkly illustrates this contrast, delineating a clear boundary line demarcating subsidence and non-subsidence regions along the border of these two provinces, which underscores the impact of groundwater management in subsidence control and the importance of proactive policy implementation.

7. Conclusions

Using integrated geodetic and hydrological data, we have investigated subsidence patterns, aquifer physical properties, and GWS changes in the NCP. Additionally, we have evaluated the contributions of the SNWD Project and groundwater management efforts in mitigating GWS depletion. This comprehensive study enhances our understanding of groundwater dynamics and highlights the pivotal role of large-scale water transfer projects and administrative interventions in addressing subsidence and resource depletion. The findings provide critical scientific support for devising more effective groundwater management policies and addressing challenges from extreme regional weather events and global climate change. Key conclusions and broader implications include:

1. *Subsidence Patterns*: For the first time, we have derived a high-resolution InSAR displacement time series for the NCP, revealing widespread and significant subsidence. The average rate is ∼29 mm/yr, with peak rates reaching up to 120 mm/yr between 2015 and 2019. This subsidence predominantly occurred in agricultural regions and near urban centers, underscoring the direct connection between intensive human activity and ground deformation. These results emphasize the urgent need for groundwater extraction policies to mitigate further subsidence and associated risks.
2. *Aquifer Property Estimation*: We have characterized key physical properties of the NCP's aquifer system, including storativity and clay lens thickness. Storativity values of the confined aquifer system range from 0.67×10^{-3} to 14.38×10^{-3} at monitoring sites, taking into account the effect of geostatic loading change. The clay lens thicknesses are estimated as $0.15 - 1.98$ m, assuming homogeneous vertical hydraulic conductivity and specific storativity for the clay lenses. These properties, closely linked to groundwater sub-region partitions, reflect the geological history of sedimentary unit formation. Understanding these spatial variations is essential for developing precise, region-specific groundwater management strategies, optimizing aquifer recharge efforts, and reducing the risk of long-term subsidence due to over-extraction.
3. *GWS Change Estimation*: Based on geodetic measurements, we have estimated the GWS change across the NCP as a continuous spatial distribution, finding strong agreement with results from analysis of other data types. Furthermore, the SNWD Project has been instrumental in mitigating GWS depletion, particularly along aqueduct routes. Between 2015 and 2019, the project accounted for a ∼1.02 km^3 increase in GWS in ∼55% of the NCP studied. This finding underscores the effectiveness of water transfer projects in alleviating regional groundwater stress and demonstrates their potential as a model for addressing water scarcity and subsidence issues in other regions.
4. *Impact of Groundwater Management*: Long-term surface deformation analysis reveals significant disparities in subsidence between provinces, highlighting the impact of groundwater management policies. Hebei Province experienced pronounced subsidence during 2015–2019, while Shandong Province, with stricter groundwater usage regulations, saw minimal subsidence. These results illustrate the tangible impact of governance on resource sustainability and stress the need for consistent and enforceable policies across regions.

Our study, conducted over a 4-year period from 2015 to 2019 using a two-layer aquifer model constrained by geodetic and hydrological measurements, has provided a framework to study aquifer properties and groundwater storage in the NCP. However, this study can still be improved on several aspects if additional data are incorporated in the analysis.

First, although geodetic measurements used in this study covered most of the NCP region, data gaps exist at the east and west margins. Incorporating SAR data from additional tracks will improve spatial coverage and enhance the monitoring of hydrological activities in the NCP. Second, extending the temporal coverage by including post-2019 data will enable future validation as more measurements become available over extended temporal and spatial scales. Increased temporal geodetic measurements will better capture long-term deformation patterns in the NCP, facilitating a more comprehensive study of the SNWD Project's impact.

Since 2019, hydrological measurements in the NCP have substantially increased, offering the potential to significantly improve estimates of aquifer physical properties and closely monitor dynamic variations in hydrological activities when combined with geodetic measurements. Continued study following the framework developed here will enhance our understanding of hydraulic processes and provide scientific support for the effective management of groundwater resources, which is critically needed in the NCP.

Data Availability Statement

The Sentinel-1 data used for this study are provided by the European Space Agency and available at the Copernicus Open Access Hub: https://scihub.copernicus.eu/dhus/#/home/. The GNSS data and hydraulic head measurement used for this study are available at: https://doi.org/10.5281/zenodo.7798617.

Acknowledgments

This research was funded by the State Key Laboratory of Earthquake Dynamics, Institute of Geology, China Earthquake Administration (No. LED2014A04, grant to J. S.), National Natural Science Foundation of China (No. 42021003, grant to L. X., No. 41774008 grant to Z. S.), Hubei Natural Science Foundation (No. 2021CFB504, grant to B. Z.) and Science and Technology Project of Beijing Earthquake Agency (No. BJMS-2022008, grant to L. H). We thank Yijian Zhou and Di Long for discussions. We appreciate Rui Yan, Minli Guo, and Wei Feng for data sharing. We also thank the editor, associate editor, and three anonymous reviewers for their comments and suggestions, which have substantially improved the manuscript.

References

Aeschbach-Hertig, W., & Gleeson, T. (2012). Regional strategies for the accelerating global problem of groundwater depletion. *Nature Geoscience*, *5*(12), 853–861. https://doi.org/10.1038/ngeo1617

Amos, C. B., Audet, P., Hammond, W. C., Bürgmann, R., Johanson, I. A., & Blewitt, G. (2014). Uplift and seismicity driven by groundwater depletion in central California. *Nature*, *509*(7501), 483–486. https://doi.org/10.1038/nature13275

Anderson, K. B., & Conder, J. A. (2011). Discussion of multicyclic Hubbert modeling as a method for forecasting future petroleum production. *Energy & Fuels*, *25*(4), 1578–1584. https://doi.org/10.1021/ef1012648

Bekaert, D., Walters, R., Wright, T., Hooper, A., & Parker, D. (2015). Statistical comparison of InSAR tropospheric correction techniques. *Remote Sensing of Environment*, *170*, 40–47. https://doi.org/10.1016/j.rse.2015.08.035

Bense, V., Van den Berg, E., & Van Balen, R. (2003). Deformation mechanisms and hydraulic properties of fault zones in unconsolidated sediments; the Roer Valley Rift System, The Netherlands. *Hydrogeology Journal*, *11*(3), 319–332. https://doi.org/10.1007/s10040-003-0262-8

Cai, X. (2008). Water stress, water transfer and social equity in northern China—Implications for policy reforms. *Journal of Environmental Management*, *87*(1), 14–25. https://doi.org/10.1016/j.jenvman.2006.12.046

Cao, G., Zheng, C., Scanlon, B. R., Liu, J., & Li, W. (2013). Use of flow modeling to assess sustainability of groundwater resources in the North China Plain. *Water Resources Research*, *49*(1), 159–175. https://doi.org/10.1029/2012WR011899

Chaussard, E., Bürgmann, R., Shirzaei, M., Fielding, E. J., & Baker, B. (2014). Predictability of hydraulic head changes and characterization of aquifer-system and fault properties from InSAR-derived ground deformation. *Journal of Geophysical Research: Solid Earth*, *119*(8), 6572–6590. https://doi.org/10.1002/2014JB011266

Chaussard, E., Milillo, P., Bürgmann, R., Perissin, D., Fielding, E. J., & Baker, B. (2017). Remote sensing of ground deformation for monitoring groundwater management practices: Application to the Santa Clara Valley during the 2012–2015 California drought. *Journal of Geophysical Research: Solid Earth*, *122*(10), 8566–8582. https://doi.org/10.1002/2017JB014676

Chen, J., Knight, R., Zebker, H. A., & Schreüder, W. A. (2016). Confined aquifer head measurements and storage properties in the San Luis Valley, Colorado, from spaceborne InSAR observations. *Water Resources Research*, *52*(5), 3623–3636. https://doi.org/10.1002/2015wr018466

Daniel, D. E. (1989). In situ hydraulic conductivity tests for compacted clay. *Journal of Geotechnical Engineering*, *115*(9), 1205–1226. https://doi.org/10.1061/(ASCE)0733-9410(1989)115:9(120

Deng, Q.-D. (2003). Active tectonics and earthquake activities in China (in Chinese). *Earth Science Frontiers*, *10*(1), 66.

Farr, T. G., Rosen, P. A., Caro, E., Crippen, R., Duren, R., Hensley, S., et al. (2007). The shuttle radar topography mission. *Reviews of Geophysics*, *45*(2), RG2004. https://doi.org/10.1029/2005RG000183

Faunt, C. C., Sneed, M., Traum, J., & Brandt, J. T. (2016). Water availability and land subsidence in the Central Valley, California, USA. *Hydrogeology Journal*, *24*(3), 675–684. https://doi.org/10.1007/s10040-015-1339-x

Feng, W., Shum, C., Zhong, M., & Pan, Y. (2018). Groundwater storage changes in China from satellite gravity: An overview. *Remote Sensing*, *10*(5), 674. https://doi.org/10.3390/rs10050674

Feng, W., Zhong, M., Lemoine, J.-M., Biancale, R., Hsu, H.-T., & Xia, J. (2013). Evaluation of groundwater depletion in North China using the Gravity Recovery and Climate Experiment (GRACE) data and ground-based measurements. *Water Resources Research*, *49*(4), 2110–2118. https://doi.org/10.1002/wrcr.20192

Ferretti, A., Prati, C., & Rocca, F. (2000). Nonlinear subsidence rate estimation using permanent scatterers in differential SAR interferometry. *IEEE Transactions on Geoscience and Remote Sensing*, *38*(5), 2202–2212. https://doi.org/10.1109/36.868878

Ferretti, A., Prati, C., & Rocca, F. (2001). Permanent scatterers in SAR interferometry. *IEEE Transactions on Geoscience and Remote Sensing*, *39*(1), 8–20. https://doi.org/10.1109/36.898661

Freeze, R. A., & Cherry, J. A. (1979). *Groundwater*. Prentice Hall.

Gao, M., Gong, H., Chen, B., Zhou, C., Liu, K., & Shi, M. (2015). Mapping and characterization of land subsidence in Beijing Plain caused by groundwater pumping using the Small Baseline Subset (SBAS) InSAR technique. *Proceedings of the International Association of Hydrological Sciences*, *372*(372), 347–349. https://doi.org/10.5194/piahs-372-347-2015

Gong, H., Pan, Y., Zheng, L., Li, X., Zhu, L., Zhang, C., et al. (2018). Long-term groundwater storage changes and land subsidence development in the North China Plain (1971–2015). *Hydrogeology Journal*, *26*(5), 1417–1427. https://doi.org/10.1007/s10040-018-1768-4

Grisak, G., & Cherry, J. (1975). Hydrologic characteristics and response of fractured till and clay confining a shallow aquifer. *Canadian Geotechnical Journal*, *12*(1), 23–43. https://doi.org/10.1139/t75-003

Herrera-García, G., Ezquerro, P., Tomás, R., Béjar-Pizarro, M., López-Vinielles, J., Rossi, M., et al. (2021). Mapping the global threat of land subsidence. *Science*, *371*(6524), 34–36. https://doi.org/10.1126/science.abb8549

Herring, T., King, R., & McClusky, S. (2010). *Introduction to GAMIT/GLOBK*. Massachusetts Institute of Technology.

Hersbach, H., Bell, B., Berrisford, P., Hirahara, S., Horányi, A., Muñoz-Sabater, J., et al. (2020). The ERA5 global reanalysis. *Quarterly Journal of the Royal Meteorological Society*, *146*(730), 1999–2049. https://doi.org/10.1002/qj.3803

Hooper, A., Bekaert, D., Spaans, K., & Arıkan, M. (2012). Recent advances in SAR interferometry time series analysis for measuring crustal deformation. *Tectonophysics*, *514–517*, 1–13. https://doi.org/10.1016/j.tecto.2011.10.013

Hooper, A., Segall, P., & Zebker, H. (2007). Persistent scatterer interferometric synthetic aperture radar for crustal deformation analysis, with application to Volcán Alcedo, Galápagos. *Journal of Geophysical Research*, *112*(B7), B07407. https://doi.org/10.1029/2006jb004763

Hooper, A., Zebker, H., Segall, P., & Kampes, B. (2004). A new method for measuring deformation on volcanoes and other natural terrains using InSAR persistent scatterers. *Geophysical Research Letters*, *31*(23), L23611. https://doi.org/10.1029/2004gl021737

Hu, X., & Bürgmann, R. (2020). Aquifer deformation and active faulting in salt lake valley, Utah, USA. *Earth and Planetary Science Letters*, *547*, 116471. https://doi.org/10.1016/j.epsl.2020.116471

Hu, X., Lu, Z., & Wang, T. (2018). Characterization of hydrogeological properties in salt Lake Valley, Utah, using InSAR. *Journal of Geophysical Research: Earth Surface*, *123*(6), 1257–1271. https://doi.org/10.1029/2017jf004497

Hung, W.-C., Hwang, C., Liou, J.-C., Lin, Y.-S., & Yang, H.-L. (2012). Modeling aquifer-system compaction and predicting land subsidence in central Taiwan. *Engineering Geology*, *147*, 78–90. https://doi.org/10.1016/j.enggeo.2012.07.018

Jain, M., Fishman, R., Mondal, P., Galford, G. L., Bhattarai, N., Naeem, S., et al. (2021). Groundwater depletion will reduce cropping intensity in India. *Science Advances*, *7*(9), eabd2849. https://doi.org/10.1126/sciadv.abd2849

Jasechko, S., Seybold, H., Perrone, D., Fan, Y., Shamsudduha, M., Taylor, R. G., et al. (2024). Rapid groundwater decline and some cases of recovery in aquifers globally. *Nature*, *625*(7996), 715–721. https://doi.org/10.1038/s41586-023-06879-8

Jiang, L., Bai, L., Zhao, Y., Cao, G., Wang, H., & Sun, Q. (2018). Combining InSAR and hydraulic head measurements to estimate aquifer parameters and storage variations of confined aquifer system in Cangzhou, North China Plain. *Water Resources Research*, *54*(10), 8234–8252. https://doi.org/10.1029/2017wr022126

Kruseman, G. P., De Ridder, N. A., & Verweij, J. M. (1970). *Analysis and evaluation of pumping test data* (Vol. 11). International institute for land reclamation and improvement, Wageningen.

Leake, S., & Galloway, D. L. (2007). *MODFLOW ground-water model: User guide to the subsidence and aquifer-system compaction package (SUB-WT) for water-table aquifers*. US Geological Survey.

Li, M., Sun, J., Xue, L., Shen, Z., Zhao, B., & Hu, L. (2022). Characterization of aquifer system and groundwater storage change due to South-to-North Water diversion project at Huairou groundwater reserve site, Beijing, China, using geodetic and hydrological data. *Remote Sensing*, *14*(15), 3549. https://doi.org/10.3390/rs14153549

Li, S., Liu, L., Zheng, F., & Jinag, J. (2011). Numerical evaluation of aquifer heat load capacity on groundwater heatpump and its utilization: By a Case of Beijing Plain. *Geoscience*, *25*(2), 370–376.

Liu, C., & Xia, J. (2004). Water problems and hydrological research in the Yellow River and the Huai and Hai River basins of China. *Hydrological Processes*, *18*(12), 2197–2210. https://doi.org/10.1002/hyp.5524

Liu, C., Zhao, G., Kong, L., Fan, C., & Fan, J. (2018). Observation error and test method of digital pressure type water level instrument. *Joural of Geodesy and Geodynamics*, *38*(1), 97–101.

Liu, C., & Zheng, H. (2002). South-to-north water transfer schemes for China. *International Journal of Water Resources Development*, *18*(3), 453–471. https://doi.org/10.1080/0790062022000006934

Liu, P., Li, Q., Li, Z., Hoey, T., Liu, G., Wang, C., et al. (2016). Anatomy of subsidence in Tianjin from time series InSAR. *Remote Sensing*, *8*(3), 266. https://doi.org/10.3390/rs8030266

Liu, R., Zhong, B., Li, X., Zheng, K., Liang, H., Cao, J., et al. (2022). Analysis of groundwater changes (2003–2020) in the North China Plain using geodetic measurements. *Journal of Hydrology: Regional Studies*, *41*, 101085. https://doi.org/10.1016/j.ejrh.2022.101085

Long, D., Yang, W., Scanlon, B. R., Zhao, J., Liu, D., Burek, P., et al. (2020). South-to-North water diversion stabilizing Beijing's groundwater levels. *Nature Communications*, *11*(1), 3665. https://doi.org/10.1038/s41467-020-17428-6

Meng, S., Fei, Y., Zhang, Z., Qian, Y., & Li, Y. (2011). Groundwater vulnerability assessment of North China Plain. *Geology in China*, *38*(6), 1607–1613.

Motagh, M., Shamshiri, R., Haghighi, M. H., Wetzel, H.-U., Akbari, B., Nahavandchi, H., et al. (2017). Quantifying groundwater exploitation induced subsidence in the Rafsanjan plain, southeastern Iran, using InSAR time-series and in situ measurements. *Engineering Geology*, *218*, 134–151. https://doi.org/10.1016/j.enggeo.2017.01.011

Ohenhen, L. O., Shirzaei, M., & Barnard, P. L. (2024). Slowly but surely: Exposure of communities and infrastructure to subsidence on the US east coast. *PNAS nexus*, *3*(1), pgad426. https://doi.org/10.1093/pnasnexus/pgad426

Poland, J. F., & Davis, G. H. (1969). Land subsidence due to withdrawal of fluids*. In D. J. Varnes & G. Kiersch (Eds.), *Reviews in Engineering Geology* (Vol. 2, pp. 0–269). Geological Society of America. https://doi.org/10.1130/REG2-p187

Poland, J. F., & Ireland, R. (1988). *Land subsidence in the Santa Clara valley, California, as of 1982* (Vol. 497). Department of the Interior, US Geological Survey. https://doi.org/10.3133/pp497f

Riley, F. S. (1970). Analysis of borehole extensometer data from central California. In *Land subsidence: Proceedings of the Tokyo Symposium* (Vol. 1, pp. 423–431). International Association of Scientific Hydrology.

Rodell, M., & Reager, J. T. (2023). Water cycle science enabled by the GRACE and GRACE-FO satellite missions. *Nature Water*, *1*(1), 47–59. https://doi.org/10.1038/s44221-022-00005-0

Rousseau-Gueutin, P., Love, A., Vasseur, G., Robinson, N., Simmons, C., & De Marsily, G. (2013). Time to reach near-steady state in large aquifers. *Water Resources Research*, *49*(10), 6893–6908. https://doi.org/10.1002/wrcr.20534

Schmidt, D. A., & Bürgmann, R. (2003). Time-dependent land uplift and subsidence in the Santa Clara valley, California, from a large interferometric synthetic aperture radar data set. *Journal of Geophysical Research*, *108*(B9). https://doi.org/10.1029/2002JB002267

Sharma, B., Rishi, D., Mudai, B., & Bhattacharjya, R. (2017). Influence of clay lens on contaminant transport in unconfined coastal aquifers. *European Water*, *58*, 359–364.

Shen, Z. K., Jackson, D. D., & Ge, B. X. (1996). Crustal deformation across and beyond the Los Angeles basin from geodetic measurements. *Journal of Geophysical Research*, *101*(B12), 27957–27980. https://doi.org/10.1029/96JB02544

Shen, Z. K., & Liu, Z. (2020). Integration of GPS and InSAR data for Resolving 3-dimensional crustal deformation. *Earth and Space Science*, *7*(4), e2019EA001036. https://doi.org/10.1029/2019ea001036

Shen, Z. K., Wang, M., Zeng, Y., & Wang, F. (2015). Optimal interpolation of spatially discretized geodetic data. *Bulletin of the Seismological Society of America*, *105*(4), 2117–2127. https://doi.org/10.1785/0120140247

Shi, M., Gong, H., Gao, M., Chen, B., Zhang, S., & Zhou, C. (2020). Recent ground subsidence in the North China Plain, China, revealed by sentinel-1A datasets. *Remote Sensing*, *12*(21), 3579. https://doi.org/10.3390/rs12213579

Shirzaei, M., Freymueller, J., Törnqvist, T. E., Galloway, D. L., Dura, T., & Minderhoud, P. S. (2021). Measuring, modelling and projecting coastal land subsidence. *Nature Reviews Earth & Environment*, *2*(1), 40–58. https://doi.org/10.1038/s43017-020-00115-x

St, L., & Wold, S. (1989). Analysis of variance (ANOVA). *Chemometrics and Intelligent Laboratory Systems*, *6*(4), 259–272. https://doi.org/10.1016/0169-7439(89)80095-4

Su, G., Xiong, C., Zhang, G., Wang, Y., Shen, Q., Chen, X., et al. (2023). Coupled processes of groundwater dynamics and land subsidence in the context of active human intervention, a case in Tianjin, China. *Science of the Total Environment*, *903*, 166803. https://doi.org/10.1016/j.scitotenv.2023.166803

Terzaghi, K. (1925). Principles of soil mechanics, IV—Settlement and consolidation of clay. *Engineering News-Record*, *95*(3), 874–878.

Tymofyeyeva, E., & Fialko, Y. (2015). Mitigation of atmospheric phase delays in InSAR data, with application to the eastern California shear zone. *Journal of Geophysical Research: Solid Earth*, *120*(8), 5952–5963. https://doi.org/10.1002/2015jb011886

Wang, D., Zhao, B., Li, Y., Yu, J., Chen, Y., & Zhou, X. (2022). Determination of tectonic and nontectonic vertical motion rates of the North China Craton using dense GPS and GRACE data. *Journal of Asian Earth Sciences*, *236*, 105314. https://doi.org/10.1016/j.jseaes.2022.105314

Wang, K., & Fialko, Y. (2018). Observations and modeling of Coseismic and Postseismic deformation due to the 2015 Mw7.8 Gorkha (Nepal) earthquake. *Journal of Geophysical Research: Solid Earth*, *123*(1), 761–779. https://doi.org/10.1002/2017jb014620

Watto, M. A., & Mugera, A. W. (2016). Groundwater depletion in the Indus Plains of Pakistan: Imperatives, repercussions and management issues. *International Journal of River Basin Management*, *14*(4), 447–458. https://doi.org/10.1080/15715124.2016.1204154

Werner, C., Wegmüller, U., Strozzi, T., & Wiesmann, A. (2000). Gamma SAR and interferometric processing software. In *Proceedings of the ERS-ENVISAT Symposium, Gothenburg, Sweden*.

Wilson, A. M., & Gorelick, S. (1996). The effects of pulsed pumping on land subsidence in the Santa Clara Valley, California. *Journal of Hydrology*, *174*(3–4), 375–396. https://doi.org/10.1016/0022-1694(95)02722-X

Xu, J., & Ji, F. (2015). *Structure and evolution of the Bohai Bay basin*. Seismological Press.

Yang, H., Cao, W., Zhi, C., Li, Z., Bao, X., Ren, Y., et al. (2021). Evolution of groundwater level in the North China Plain in the past 40 years and suggestions on its overexploitation treatment. *Geology in China*, *48*(4), 1142–1155. https://doi.org/10.12029/gc20210411

Yao, C., Lu, C., Qin, W., & Lu, J. (2019). Field experiments of hyporheic flow affected by a clay lens. *Water*, *11*(8), 1613. https://doi.org/10.3390/w11081613

Zhang, C., Duan, Q., Yeh, P. J. F., Pan, Y., Gong, H., Gong, W., et al. (2020). The effectiveness of the South-to-North Water diversion Middle route project on water delivery and groundwater recovery in North China plain. *Water Resources Research*, *56*(10), e2019WR026759. https://doi.org/10.1029/2019WR026759

Zhang, J., Hu, L., Sun, J., & Wang, D. (2023). Reconstructing groundwater storage changes in the North China Plain using a numerical model and GRACE data. *Remote Sensing*, *15*(13), 3264. https://doi.org/10.3390/rs15133264

Zhang, Y., Lei, H., Zhao, W., Shen, Y., & Xiao, D. (2018). Comparison of the water budget for the typical cropland and pear orchard ecosystems in the North China Plain. *Agricultural Water Management*, *198*, 53–64. https://doi.org/10.1016/j.agwat.2017.12.027

Zhang, Y., Ying, G., Yanjun, S., Yongqing, Q., & Jianmei, L. (2020). Impact of planting structure changes on agricultural water requirement in North China Plain. *Chinese Journal of Eco-Agriculture*, *28*(1), 8–16. https://doi.org/10.13930/j.cnki.cjea.190490

Zhang, Z., Fei, Y., Chen, Z., Zhao, Z., Xie, Z., Wang, Y., et al. (2009). Investigation and assessment of sustainable utilization of groundwater resources in the North China Plain. *Geological Publishing House*.

Zhang, Z., Luo, G., Wang, Z., Liu, C., Li, Y., & Jiang, X. (2009). Study on sustainable utilization of groundwater in North China Plain. *Resources Science*, *31*(3), 355–360.

Zhao, B., Zhang, C., Wang, D., Huang, Y., Tan, K., Du, R., & Liu, J. (2017). Contemporary kinematics of the Ordos block, North China and its adjacent rift systems constrained by dense GPS observations. *Journal of Asian Earth Sciences*, *135*, 257–267. https://doi.org/10.1016/j.jseaes.2016.12.045

Zhao, Q., Zhang, B., Yao, Y., Wu, W., Meng, G., & Chen, Q. (2019). Geodetic and hydrological measurements reveal the recent acceleration of groundwater depletion in North China Plain. *Journal of Hydrology*, *575*, 1065–1072. https://doi.org/10.1016/j.jhydrol.2019.06.016